Super-hard and anti-corrosion (AlCrMoSiTi)N$_x$ high entropy nitride coatings by multi-arc cathodic vacuum magnetic filtration deposition

Yiman Zhao [a], Shunian Chen [b], Yujie Chen [a,c], Shuai Wu [a], Wenling Xie [a], Weiqing Yan [b], Shu Wang [a], Bin Liao [b,*], Sam Zhang [a,**]

[a] Center for Advanced Thin Films and Devices, School of Materials and Energy, Southwest University, Chongqing, 400715, China
[b] Key Laboratory of Beam Technology of Ministry of Education, College of Nuclear Science and Technology, Beijing Normal University, Beijing, 100875, China
[c] School of Mechanical Engineering, The University of Adelaide, Adelaide, SA, 5005, Australia

ARTICLE INFO

ABSTRACT

Super-hard and corrosion-resistant (AlCrMoSiTi)N$_x$ high-entropy nitride coatings were prepared using a novel multi-arc cathodic vacuum magnetic filtration deposition at different N$_2$ gas flow rates (R$_N$) of 0, 20, 50 and 70 sccm. The influence of R$_N$ on the element composition, phase structure, mechanical, tribological and corrosion properties of the coatings were systematically studied. Higher R$_N$ promoted higher N contents in the coatings that resulted in a transformation from an amorphous to face-centered-cubic (FCC) phase. At a high N content of 49 at. % (R$_N$ = 70%), the coating exhibits a simple FCC structure, and offers a superior combination of super-hardness, excellent wear and corrosion resistance. The exceptional hardness of the (AlCrMoSiTi)N coating (41.6 GPa) that surpasses most high-entropy ceramics is underlain by the formation of strong metal-nitride phase, the solid-solution strengthening and the fine grain strengthening. Therefore, (AlCrMoSiTi)N$_x$ nitride coating presents a potential application in protective coating owing to its extraordinary mechanical properties and corrosion resistance.

1. Introduction

Traditional binary and ternary nitride coatings (such CrN, TiN, TiAlN, and etc.) which possess good wear resistance, outstanding mechanical properties, excellent corrosion resistance, and etc., were widely applied as protective coatings on mechanical tools and parts [1,2]. However, with the rapid development of the machining industry, these nitride coatings have been unable to meet the increasingly harsh working environment. Therefore, a more effective protective coating should be produced. In past decade, high-entropy alloys nitride coatings, which possessed high hardness [3], excellent wear resistance [4], outstanding thermal stability [5], good corrosion resistance [6] and irradiation resistance [7], have attracted huge interest.

High-entropy alloy (HEA) was innovatively proposed by Yeh [8] and Contor [9] in 2004. HEA contains more than 5 and less than 13 elements, and the atomic percentage (at. %) of each element is controlled within 5–35% [10]. Furthermore, HEA nitride coatings which based on HEA can be prepared through reactive coating technique, that is, during the deposition process, the atoms or ions from the target are allowed to react with N$_2$-containing Ar flow. Thus, such HEA nitride coatings possess four core effects: high entropy effects, severe lattice distortion, sluggish diffusion and cocktail effects [11]. Besides, owing to the combination of high entropy effect and solid solution effect of binary nitrides, HEA nitride coatings present a simple solid-solution phase with body-centered cubic (BCC), face-centered cubic (FCC) or even amorphous rather than the intermetallic compounds [12–14].

The attainment of high hardness is a vital requirement for protective coatings operated in harsh environments. The wear resistance of a hard coating has a strong scaling relationship with its hardness. Therefore, enhancing the coating hardness not only improves the performance, but also extends the service life of engineering components, thus, reducing maintenance and replacement costs. The elements included in the HEA nitride coatings can be classified as either strong nitride-forming elements (e.g., Al, Cr, Hf, Mo, Si, Ta, Ti, V, Zr, etc.) or weak or non-nitride-forming elements (e.g., Fe, Co, Cu, Ni, Mn, etc.) [15]. HEA nitride coatings that contain high contents of weak or non-nitride formers

---

* Corresponding author.
** Corresponding author.
E-mail addresses: liaobingz@bnu.edu.cn (B. Liao), samzhang@swu.edu.cn (S. Zhang).

usually show relatively low hardness values, typically below 20 GPa. In contrast, HEA nitride coatings consist of strong nitride-forming elements can readily achieve high hardness values. However, it has been demonstrated that the hardness of most HEA nitride coatings, including those based on strong nitride formers, did not reach the superhard grade, i.e., greater than 40 GPa. Recently, (AlCrTiVZr)N film synthesized through HiPIMS exhibits ultra-high hardness of 41.8 GPa and a low wear rate of 2.3×10^{-7} mm^3/Nm [16]. However, the corrosion properties of the ultra-high hardness film had not been reported. Moreover, there are scarcely any systematic studies on the tribological and corrosion properties of super-hard HEA nitride coatings.

Vacuum arc deposition [3] and magnetron sputtering (MS) (such as direct current (DC) [17], radio frequency (RF) [15], and high-power impulse magnetron sputtering (HiPIMS) [18]), are the most common technique to produce the HEA nitride coatings. The HEA targets applied to the MS technique are usually manufactured by arc melting method [19]. However, since the melting point and mechanical properties of each target element composition are significantly different, it is relatively difficult to prepare HEA targets. In addition, the ionization rate for the MS technology is relatively low. Filtered cathodic vacuum arc (FCVA) deposition technique, which possess a 100% ionization rate, is widely applied to prepared coatings, owing to its ability to filter out most of the neutral atoms and macro ions and generate high-quality plasmas [20]. Moreover, the most obvious advantage of FCVA is that the target material can be freely chosen, and the composition can be adjusted by regulating the arc current of the targets. Zhang et al. [21] have reported on thick yet tough TiN coatings prepared by FCVA, and the coatings have high hardness and excellent wear resistance. Chen et al. [22] have synthesized the TiAlCN/TiAlN/TiAl multilayer composite coatings synthesized by FCVA at various carbon content. The microstructure of the composite coating is very dense. Compared with the coating prepared by MS, it has significantly higher hardness (44.36 GPa) and H/E value as well as excellent corrosion resistance. According to these publications, the FCVA is a promising technique to control the microstructure and enhance mechanical and physical properties of deposited coatings.

Based on factors aforementioned, a novel multi-arc cathodic vacuum magnetic filtration deposition technique, which equipped with a 120° Y-shaped magnetic filter duct, based on FCVA is used to synthesis HEA nitride coatings (Fig. 1). The target material can be freely chosen owing to the two independent cathode arc sources in this deposition system. During the deposition process, the two cathode arc sources respectively generate plasmas of corresponding elements and enter the magnetic filter. The plasma of each element enters the outlet end of the filter under the guidance of the magnetic field. During the plasma transmission process, the plasma is fully mixed and filtered. At the same time, N$_2$ is ionized, and N ions are also added to the mixing. Then, the fully mixed multi-element plasma precursor is finally uniformly deposited on the sample surface to form a HEA nitride coating which may possess excellent properties.
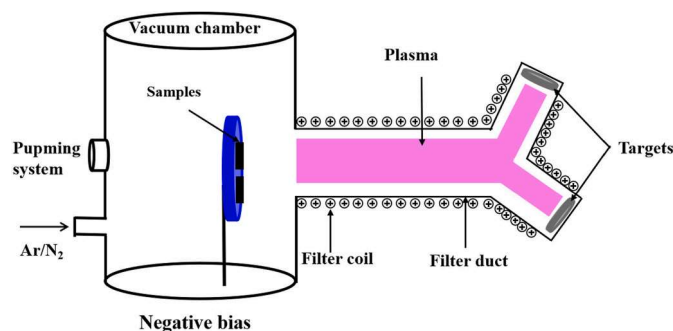
In this study, the novel multi-arc cathodic vacuum magnetic filtration deposition technique was used to synthesis HEA nitride coatings. Al, Cr, Ti, Mo and Si were chosen as the sputtering materials, owing to their strong nitride forming abilities. Using X-ray diffraction (XRD), field emission scanning electron microscopy (FESEM), tribometer, nanoindentation, and electrochemical workstation, the effect of N$_2$ gas flow rate on element composition, phase structure, hardness, tribological and corrosion properties of the (AlCrMoSiTi)N$_x$ high-entropy nitride coatings was systematically investigated and discussed.

2. Experimental

2.1. Coating preparation

The (AlCrMoSiTi)N$_x$ nitride coatings were prepared on the clean silicon wafer (20 × 20 × 1 mm), AISI 304L stainless steel (20 × 20 × 3 mm) block substrates using a multi-arc cathodic vacuum magnetic filtration deposition (Fig. 1). TiMo (50 at. % of Ti and 50 at. % of Mo, 99.80% purity) and CrAlSi (30 at. % of Cr, 60 at. % of Al and 10 at. % of Si, 99.80% purity) were chosen as the sputtering targets. The argon (Ar) and nitrogen (N$_2$) with the purity of 99.99% were used as the reaction gases. The diameter and thickness of the two targets were 100 and 20 mm, respectively. Before the deposition process, all substrates were cleaned sequentially and rinsed by acetone, alcohol, and distilled water in an ultrasonic bath for 10 min, respectively, and then dried in N$_2$ gas. Before the deposition process, the base pressure was evacuated to 5×10^{-3} Pa. In order to make the surface cleaner, all substrates were sputtering cleaned for 40 s under a pulse bias voltage of −800, −600, −400 and −200 V, respectively. During the coating deposition process, the arc current of TiMo and CrAlSi cathode was 140 and 110 A, respectively. The gas mixture composed of Ar and N$_2$ was let in the chamber at a constant total flow of 100 sccm. The Ar and N$_2$ flows were adjusted to achieve different N$_2$ flow ratios (R$_N$ = N$_2$/(N$_2$+Ar)). The substrates were not external heated during the deposition process. The thicknesses of the prepared coatings were within the ranges of 0.9–1.5 μm. The substrate temperature was around at 100 °C during the deposition process. The detailed information of the process parameters for the coating deposition were listed in Table 1.

2.2. Structure characterization

Ultraviolet photoelectron spectroscopy (UPS, ESCALAB 250 Xi) and X-ray photoelectron spectroscopy (XPS, ESCALAB 250 Xi) with a monochromatic Al Kα radiation source were employed to analyze the work function and chemical bonding of the coatings prepared on silicon. For the UPS detection, the adsorption layer on the surface of the coating was cleaned by argon atomic ion with the cleaning thickness of 20 nm. For the XPS detection, a 1000 eV Ar$^+$ ion beam was employed to sputter etch of the coatings 2 min to remove the contamination on the surface of the coatings. The base pressure was better than 5.0×10^{-9} mbar during the spectra acquisition. Residual gas analysis showed that the main background gases in the analysis chamber were argon and the spectra

Fig. 1. Schematic diagram of multi-arc cathodic vacuum magnetic filtration deposition system.

Table 1
Detailed information of the process parameters for the coating deposition.

Parameters	Coating deposition
Base pressure (Pa)	5×10^{-3}
Working pressure (Pa)	0.6
TiMo target current (A)	140
CrAlSi target current (A)	110
Ar + N$_2$ (sccm)	100
R$_N$ (N$_2$/(N$_2$+Ar)) (%)	0, 20, 50, 70
Substrate bias (V)	−50
Duty cycle (%)	100
Deposition time (min)	60

were acquired parallel mode. The electron emission angle is along the normal direction, and the spot diameter is 500 μm. The incidence angle is 70° and the charge neutralizer is used. Moreover, the Valance band spectra were measured with a monochromatic He I light source (21.2 eV) and a VG Scienta R4000 analyzer. A field emission scanning electron microscopy (FESEM, Hitachi S-4800) equipped with an energy disperse spectroscopy (EDS, EX-350) was employed to analyze the thickness and microstructure of the coatings, as well as the wear debris. An X-ray diffraction (XRD, SmartLab S2) by Cu Kα radiation with a glancing incident angle of 1° was applied to analyze the crystalline structure of the coatings. The step size of 0.02°, and 2theta range varied from 20 to 90°. The grain sizes (D) of the coatings were calculated by using the Scherrer equation: $D = (k \times \lambda)/(\beta \times \cos\theta)$ [23]. Where k is the Scherrer constant normally taken as 0.9 and it is related to the crystallite shape, λ is the wavelength of the X-ray sources (0.15406 nm), β is the full width at half maximum (FWHM) of the diffraction peak resulting from small crystallite size in radians and θ is the peak position in radians. In addition, a high-resolution transmission electron microscope (HRTEM, TF20) was used to inspect the micro-structures of the coatings. The thin films prepared under different N₂ gas flow rates were first prepared on the NaCl substrates and then gathered the suspension after the NaCl substrate had been dissolved in distilled water for the TEM observations.

2.3. Mechanical properties

A Nanoindenter G200 (Keysight Technologies) equipped with a Berkovich diamond probe tip was employed to measure the hardness (H) and Young's modulus (E) of the coatings. In order to minimize the influence of the substrate, the indentation depth was controlled to abound 80 nm (less than one-tenth of the thickness of the coatings). Moreover, the test was repeated at least 5 times to reduce the errors. A step profiler (Taylor hobson, form talysurf 50) was used to measure the curvature radius of the Si substrates before and after deposition, and the residual stress of the coatings were calculated by Stoney's equation [24]:

$$\sigma = \frac{E}{1 - \nu} \frac{t_s^2}{6t_c} \left(\frac{1}{R_1} - \frac{1}{R_0} \right)$$

where E, v, t_s, are the Young's modulus, Poisson' ratio, thickness of the Si substrate, respectively; t_c is the coating thickness; and R_0 and R_1 are the curvature radius of the Si substrate before and after coating deposition, respectively. In addition, the test was repeated at least 5 times to reduce the errors.

2.4. Tribological properties

The tribological performance of the coatings was tested at a room-temperature (RT) environment by using a ball-on-disk tribometer (MFTR-4000) in a reciprocating configuration. The Si₃N₄ ball (diameter 6 mm) was used as friction counter ball. The normal load and frequency are 1 N and 1 Hz, respectively, and the test time is 30 min. In addition, the test was repeated at least 3 times under the same experiment conditions to avoid accidental data. The step profiler was used to measure the depth and width profiles of the wear track. The wear rate (W) of the coatings was calculated by the following formula: $W = V/(F_N \times S)$ [25]. Where V is the wear volume of the wear track (mm³), F_N is the applied normal load (N) and S is the sliding distance (m).

2.5. Corrosion resistance

An electrochemical workstation (PARSTAT 2273) was applied to study the potentiodynamic polarization of the 304 SS and prepared coatings. The conventional 3-electrode system was used for electrochemical research in 3.5 wt. % NaCl solution. Saturated calomel electrode (SCE), platinum sheet and coatings were used as the reference electrode, auxiliary electrode and working electrode, respectively. Prior

to the test, the coatings were immersed in the NaCl solution for 30 min to ensure the stabilization. Then, the potentiodynamic polarization test was enforced at RT with a scan rate of 1.0 mV/s. Corrosion current density (i_{corr}) and corrosion potential (Ecorr) were obtained via the Tafel extrapolation. Each measurement was repeated 3 times to assess the scatter of the measured characteristics.

3. Results and discussion

The element compositions measured by the XPS of the (AlCrMoSiTi) Nₓ high-entropy nitride coatings prepared at various N₂ gas flow rates are shown in Fig. 2. From Fig. 2, it can be seen that the O content is around 5 at. % and changes little when the R_N increases, which may attributed to the residual oxygen in the chamber during the coating deposition process. With increasing R_N from 0 to 70%, the N content in the coatings increased linearly, and the contents of other four metal elements decrease accordingly. It is worth noting that the content of the Si element is around 3 at. % ignoring the increasing of the R_N. The low Si content could be attributed to two factors. First, the content of Si element in the sputtering target CrAlSi is as low as 10%. Second, the sputtering yields of Si element is lower than that of other target elements [26]. The N content in the nitride coatings reached a maximum value of 49 at. % when $R_N = 70\%$, which can be regarded as nitride coatings and named (AlCrMoSiTi)₅₁N₄₉ [27]. Thus, the (AlCrMoSiTi)Nₓ high-entropy nitride coatings were successfully prepared by the novel multi-arc cathodic vacuum magnetic filtration deposition.

The core energy level spectrum of Al 2p, Cr 2p, Mo 3d, Si 2p, Ti 2p, N 1s, C 1s and O 1s are shown in Fig. 3. The C 1s (Fig. 3g) was used to calibrate the XPS spectra of the other elements. According to the previous studies, the sum of C 1s peak position and sample work function is constant of 289.58 ± 0.14 eV [28–31]. The work function of the (AlCrMoSiTi)Nₓ high-entropy nitride coatings prepared at $R_N = 0\%$, 20%, 50% and 70% were 5.07, 5.23, 4.91 and 5.11, respectively. Thus, the C 1s peak positions of these nitride coatings were 284.51, 284.35, 284.67 and 284.47 eV, respectively. In the metal core energy level spectrum (see Fig. 3a–e), as the N content in the coatings increases, the peak position shifts to a higher binding energy (Eb). When R_N increases to 70%, the peak position of each element corresponding to the metallic environment shifts to the nitride position [32–34]. Moreover, as the R_N increases, the peak position of N 1s also slightly shifts to higher Eb (see Fig. 3f). The peak position for the coating deposited at $R_N = 70\%$ is ranged between 396.9 and 397.8 eV, which is between the reference
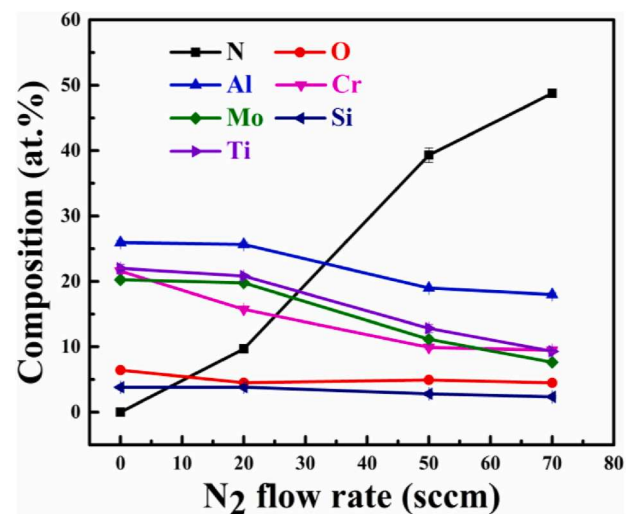

Fig. 2. Element compositions (by XPS) of the (AlCrMoSiTi)Nₓ high-entropy nitride coatings prepared at various N₂ gas flow rates. The N content in the coatings increases with increasing R_N, and the coatings were regarded as nitride coatings when $R_N = 70\%$.
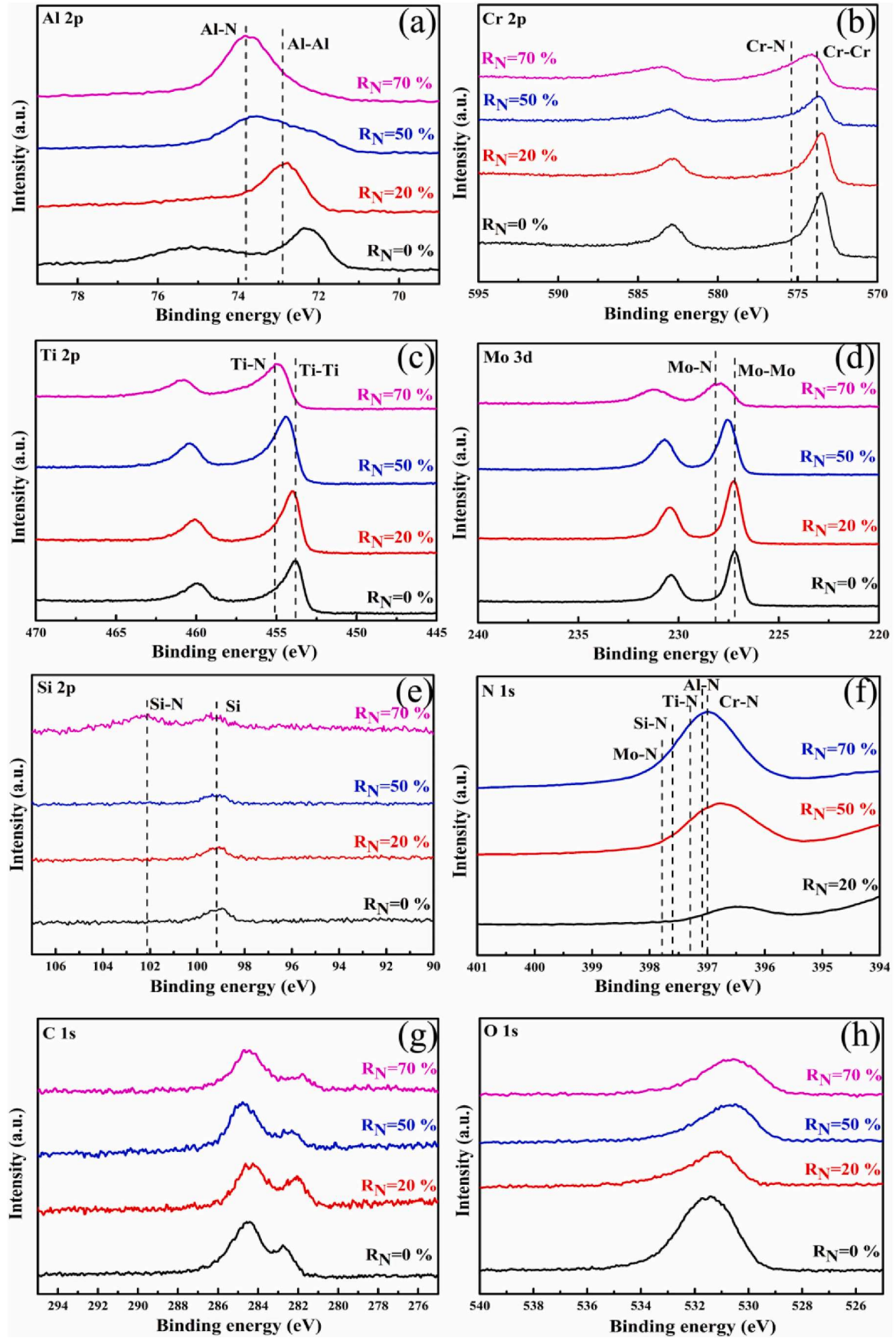
Fig. 3. XPS spectra for the (AlCrMoSiTi)N$_x$ high-entropy nitride coatings, showing the core energy levels of (a) Al 2p, (b) Cr 2p, (c)Ti 2p, (d) Mo 3d, (e) Si 2p, (f) N 1s, (g) C 1s and (h) O 1s. Peak positions of the elements shifted to higher Eb with increasing R$_N$, and all the target elements form stable nitrides when R$_N$ = 70%.

values of Al–N, Cr–N, Mo–N, Si–N and Ti–N [34], indicating that the N is in the state of nitride.

For the coatings prepared at low R_N values (0%, 20% and 50%), the peak positions in the Al 2p, Cr 2p and Mo 3d spectra (Fig. 3a–b,d) dramatically shifted to lower Eb. Compared with the respective metal reference positions, Al 2p is 72.9 eV, Cr 2p is 573.8 eV, Mo 3d is 227.2 eV, and Ti 2p is 453.8 eV [35]. In addition, the peak position of the coating prepared at R_N = 0% at 75.0 eV for Al 2p spectra may attribute to the form of Al–O bond and the overlap of the Cr 3s peak [35,36]. The presence of O could be attributed to the residual oxygen in the chamber during the coating deposition process. Moreover, for the O core energy level spectrum (Fig. 3h), the peak position of the coating prepared at R_N = 0% is observed at 531.4 eV, confirming the existence of the Al–O phase, which is consistent with the results Al 2p spectrum [35,36]. It is interesting to point that, for the coating prepared at R_N = 0%, only Al bonds with oxygen, which may due to the Al–O has a higher mixing enthalpy (ΔH = −837.9 kJ/mol) [37]. With the N content in the coatings increases, the peak position shifts to a lower Eb at about 531.0 eV, which confirms the free O [35]. The nitride coating prepared at R_N = 70% has the N content of 49 at. %, and the Al 2p, Cr 2p, Mo 3d and Ti 2p peaks are at a position of 73.8, 575.4, 228.2 and 455.1 eV, corresponding to Al–N, Cr–N, Mo–N and Ti–N reference position, respectively [35,38]. The Si 2p spectra shows two peaks which centered at 99.2 and 102.1 eV, assigning to the free Si [39] and Si–N bond [35], respectively (see Fig. 3e). The XPS spectra shows that as R_N increases, the material gradually evolves from a metallic material to a nitride material. For the coatings deposited at R_N = 70%, all the target elements form stable nitrides, which is consistent with the above results.

XRD patterns of the nitride coatings prepared under different N_2 gas flow rates are shown in Fig. 4. As seen in the XRD patterns, the coatings prepared at R_N = 0%, 20% and 50% all exhibit an amorphous structure [19], owing to the large atomic size difference (the atomic size of Al: 1.43 Å, Cr: 1.27 Å, Mo: 1.4 Å, Si: 1.34 Å and Ti: 1.45 Å) and the high mixing entropy effect of HEAs, which increases the mutual solubility of the target elements [40]. With increasing the R_N value from 0% to 50%, the center of the broad peaks in the XRD patterns gradually shifts to smaller angles, indicating that the average interatomic distance of the planes that contributes to the X-ray structural diffraction increases as the N content in the coatings increased. In addition, these peaks also gradually broaden with increasing the R_N value, that is, the degree of disorder of the amorphous structure increases. Compared with the size of interstitial sites, the size of the N atom is relatively large, therefore, the

incorporation of small N atoms at small interstitial sites would enlarge the interatomic spacing and distort the atomic configuration, so the structure of the coating is more disordered at a higher N content [41]. However, when the R_N increased to 70%, the amorphous structure transforms to a NaCl-type FCC structure. The phase structures of AlN, CrN, TiN, MoN and Si_3N_4 are HCP, FCC, FCC, HCP and amorphous, respectively [42]. Although there are differences in the phase structure of these binary nitrides, the prepared (AlCrMoSiTi)N high-entropy nitride coatings crystallized in an FCC structure. This indicates that the FCC structure resulting from the combination of the FCC-forming binary nitrides effectively accommodates the non-FCC binary nitrides. The grain sizes corresponding to each peak of the FCC phase were calculated by using the Scherrer equation [23]. The grain size corresponding to the (200) and (220) of peaks was calculated to be 6.91 and 5.66 nm, respectively, thus, the averaged grain size is ~6.3 nm. It means that as the R_N value increases, the phase structure changed from amorphous to a nanocrystalline structure with extremely small grain size. Similar results have been reported on $(AlCrMnMoNiZrB_{0.1})N_x$ [40], $(AlCrMoTaTi)N_x$ [43] and $(AlCrTaVZr)N_x$ [20] nitride coating systems.

The TEM images of the $(AlCrMoSiTi)N_x$ high-entropy nitride coatings prepared at R_N of (a) 0% and (b) 70% are shown in Fig. 5a and (b), respectively. The AlCrMoSiTi coating without N doped is shown to be amorphous from the featureless bright field image (Fig. 5a). For the (AlCrMoSiTi)N coating with high N content of 49 at. %, it can be seen that some regions (yellow-dotted lines) are crystalline structure, which can reach 2–3 nm. This feature indicates that the grain size reaches the nanocrystalline level, which confirms the above results of the XRD analysis. The results were similar to the report by Chang et al. [41].

The FESEM cross sections for $(AlCrMoSiTi)N_x$ high-entropy nitride coatings prepared at various N_2 gas flow rates are illustrated in Fig. 6. For the HEA metal coating (Fig. 6a), there exist some dimple fractures in the middle part of the coating, which would occur during the sample preparation process, and the specific reasons may require further analysis. Despite this phenomenon, the cross section is uniform and dense without pores and defects. For the nitride coatings (Fig. 6b–d), it can be seen that the cross-sectional images for all the coatings shown a dense and smooth structure without large particles, visible pores and voids, because large particles were magnetron filtered during the deposition [44–47]. Moreover, all the coatings are well combined with the substrates, and there are no defects and cracks at the interface. Excellent corrosion resistance can be expected in $(AlCrMoSiTi)N_x$ nitride coatings with dense and smooth structure.

The mechanical properties, including hardness (H), residual stress, Young's modulus (E), H^3/E^2 and H/E of $(AlCrMoSiTi)N_x$ nitride coatings are shown in Fig. 7 and Table 2, respectively. For the HEA metal coating without the addition of N, the H and E are 12.0 GPa and 169.7 GPa, respectively. As the R_N increases, both the H and E of the nitride coatings increase from 14.8 to 41.6 GPa and 192.3–372.6 GPa, respectively. When R_N = 70%, the N content in the coating reaches a maximum of 49 at. %, and the H and E of the coating rises up to 41.6 GPa and 372.6 GPa, respectively. The super-hard level hardness can mainly be attributed to the following three factors. First, with the inclusion of a high content of strong nitride forming elements, the formation of strong metal-nitrogen bonding of nitrides can effectively increase the hardness of the HEA nitride coatings [48]. Second, the interstitial solid solution strengthening induced by the incorporation of N atoms. Third, the residual stress of the coatings is increased with R_N increasing. According to the previous studies, the hardness is the resistance to local plastic deformation that produces the stress field itself. Therefore, the hardness increases by a residual stress [36,49]. Finally, the grain boundary strengthening caused by the extremely fine nanograined structure. It is well known that materials become harder with reducing grain sizes, following the classical Hall-Petch effect [50]. The average grain size of the (AlCrMoSiTi)N coating was estimated to be ~6.3 nm. Such a fine grain size can significantly enhance the hardness. During the deposition process of multi-arc cathodic vacuum magnetic filtration, the grown crystals were
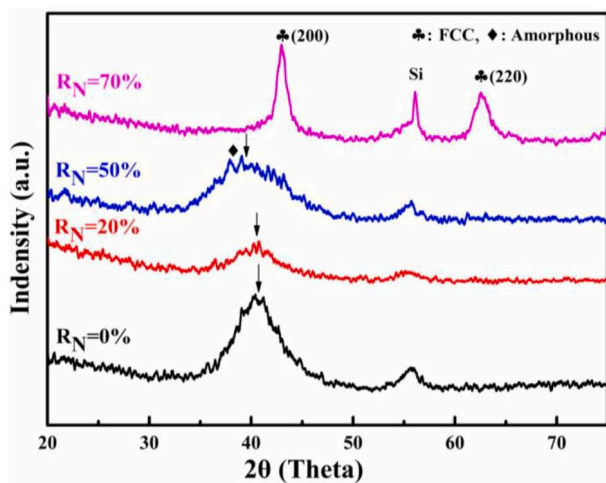

Fig. 4. XRD patterns of $(AlCrMoSiTi)N_x$ high-entropy nitride coatings prepared at various N_2 gas flow rates. The amorphous structure transforms to the NaCl-type FCC structure with the R_N increased to 70%, owing to the FCC-forming binary nitrides effectively accommodates non-FCC binary nitrides.
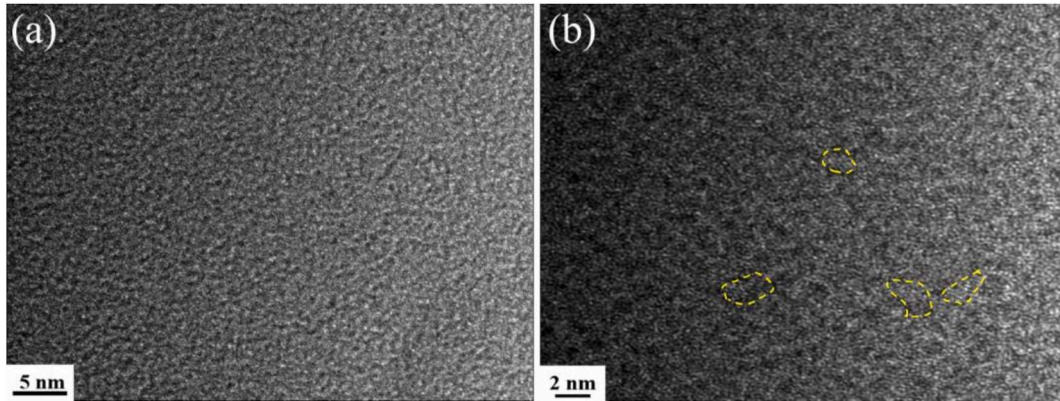
Fig. 5. TEM bright field images of (AlCrMoSiTi)N$_x$ high-entropy nitride coatings prepared at R$_N$ of (a) 0% and (b) 70%. The coating prepared at R$_N$ = 0% presents an amorphous structure, and the coating prepared at R$_N$ = 70% tends to be crystalline.
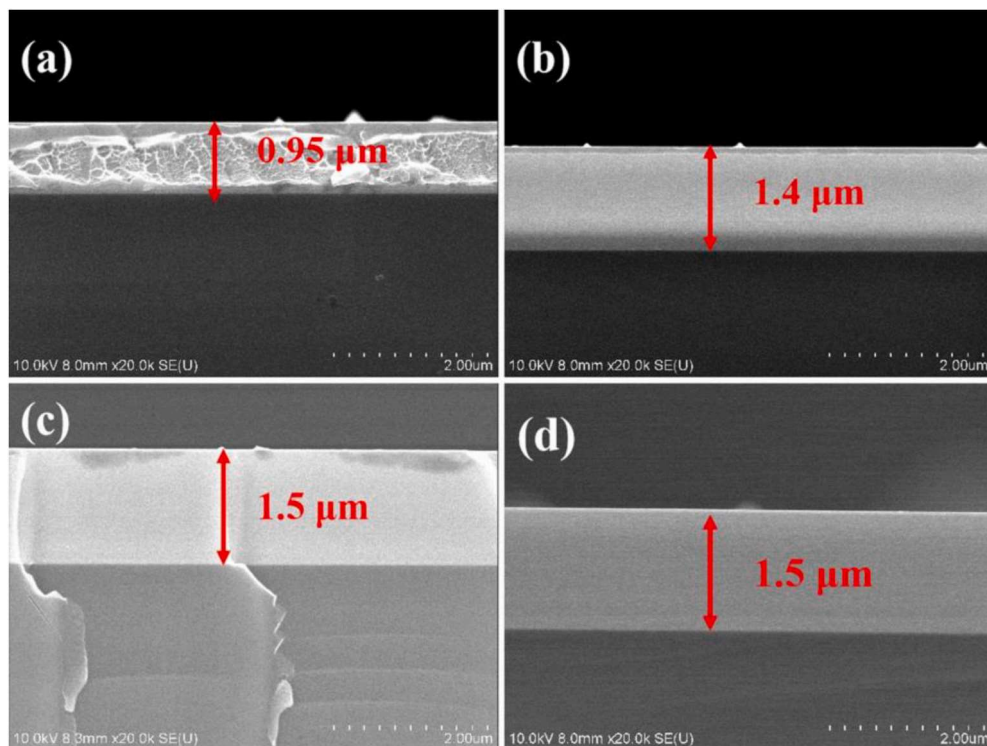

Fig. 6. The FESEM cross sections for (AlCrMoSiTi)N$_x$ high-entropy nitride coatings prepared at various N$_2$ gas flow rates: (a): 0%; (b): 20%; (c): 50%; (d): 70%. The cross-sectional images for all the coatings shown a dense and smooth structure without large particles, visible pores and voids, which are important for corrosion resistance.

periodically bombarded by high-energy ions, refining the large crystal grains. At the same time, the reaction gas (Ar and N$_2$) is stably controlled to produce the (AlCrMoSiTi)N$_x$ high-entropy nitride coatings with dense structure and good mechanical properties. Thus, the hardness of the (AlCrMoSiTi)N nitride coatings prepared by multi-arc cathodic vacuum magnetic filtration deposition in this study is higher than that of the nitride coatings with similar composition prepared by MS, which is around 30 GPa [42,43]. Besides, the hardness of the (AlCrMoSiTi)N high-entropy nitride coating is also much higher than that of most HEA nitride coatings, including TiVCrZrHf [51], FeMnNiCoCr [25], AlCrMnMoNiZr [52], and CrTaNbMoV [27] nitride coatings, and similar to that of AlCrTiVZr [16], AlCrMoTaTiZr [53], AlCrNbSiTiV [54], TiZrNbAlYCr [55] and TiHfZrVNb [56] nitride coatings.

It is known that the H/E ratio reflects the wear resistance of coatings [57]. Coatings with higher H/E ratios are more wear resistant. In addition, the H^3/E^2 ratio represents the ability of the coating to resist plastic deformation. A higher H^3/E^2 ratios indicate that the coating has a higher resistance to plastic deformation [22,58]. As shown in Fig. 7b, with the increase of the R$_N$ value, both the H/E and H^3/E^2 values increase from 0.07 to 0.11 and 0.06 to 0.49, respectively. When R$_N$ = 70%, the H/E and H^3/E^2 ratio of the coating reach the maximum values of 0.11 and 0.49, respectively, which were higher than those of coatings prepared by other techniques (such as RF and DC) [33,52]. Higher H/E and H^3/E^2 values of the coating also indicates its excellent resistance to wear and plastic deformation. As mentioned above, the crystal grain sizes are extremely fine owing to the periodically bombarded by high-energy ions during the deposition process. Simultaneously, the reaction gas (Ar and N$_2$) is stably controlled to produce the (AlCrMoSiTi)N$_x$ nitride coatings with dense structure and good mechanical properties.
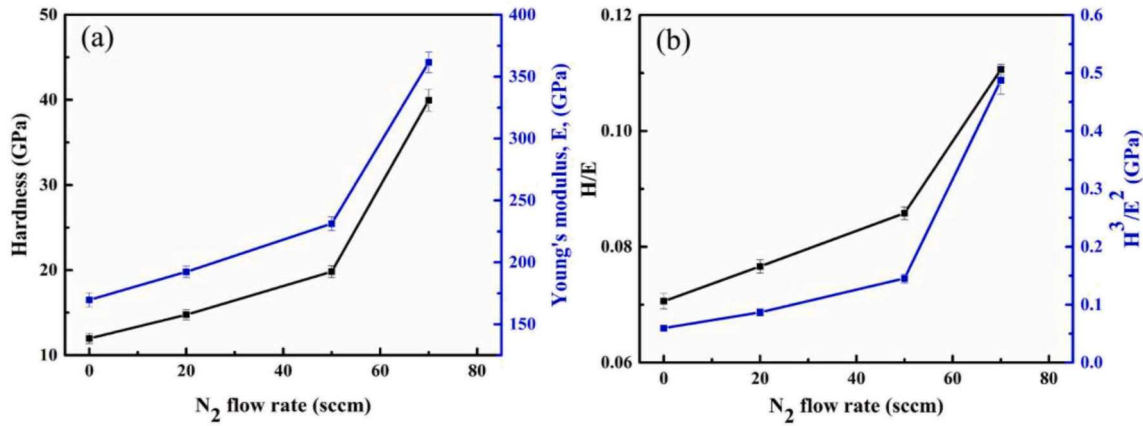
Fig. 7. Mechanical properties of the (AlCrMoSiTi)N$_x$ high-entropy nitride coatings as a function of N$_2$ gas flow rate: (a) H and E and (b) H/E and H^3/E^2. The hardness of the coating deposited at R$_N$ = 70% rises up to 41.6 GPa, due to the formation of strong nitrides, the solid solution strengthening and the fine grain strengthening.

Table 2
Summary of mechanical and tribological properties of (AlCrMoSiTi)N$_x$ high-entropy nitride coatings prepared at various N$_2$ gas flow rates.

R$_N$ (%)	Hardness (GPa)	Residual stress (GPa)	Friction coefficient	Wear rate (10^{-6} mm^3 N^{-1} m^{-1})
0	11.97 ± 0.59	−0.5	0.53	28.96
20	14.75 ± 0.58	−1.7	0.55	5.41
50	19.81 ± 0.69	−3.0	0.52	3.25
70	41.60 ± 1.27	−4.6	0.51	3.19

The friction coefficient curves for the (AlCrMoSiTi)N$_x$ nitride coatings deposited under various N$_2$ gas flow rates sliding against Si$_3$N$_4$ balls are shown in Fig. 8. It has shown that the friction coefficient curves of all samples increased dramatically in the initial stage, which corresponding to the run-in period, and then quickly reached a relatively steady state. The average friction coefficient of all coatings remains around 0.5, indicating that the R$_N$ has little influence on the friction coefficient of the (AlCrMoSiTi)N$_x$ high-entropy nitride coatings. The friction coefficient and wear rate of the (AlCrMoSiTi)N$_x$ high-entropy nitride coatings are listed in Table 2. The wear rate of the coatings decreases dramatically with the increases of R$_N$, and reaches the minimum value of about 3.19 × 10^{-6} mm^3/Nm at R$_N$ = 70%. As mentioned above, the wear resistance

of coatings is evidently influenced by the value of the hardness and the H/E ratio. Thus, the decrease in the wear rate is mainly owing to the increases in the coatings' hardness and H/E.

Fig. 9 shows the wear tracks of (AlCrMoSiTi)N$_x$ high-entropy nitride coatings after sliding in the atmosphere. The long wear scars with deep grooves and adhered materials observed in the wear tracks of the coatings deposited at low R$_N$ values (Fig. 9a and b) indicate that their wear behavior was dominated by the abrasive wear, due to their relatively low hardness. The wear track of the coating prepared at intermediate R$_N$ values (Fig. 9c) is relatively smooth and exhibit fewer grooves and cracks. The coatings with 49 at. % N shows a mild wear feature, and the wear track is smooth and with scarcely any grooves. As mentioned above, the wear resistance of coatings is closely related to the value of the hardness and the H/E ratio, which reflect the resistance to abrasion wear [59]. Thus, the coatings prepared at intermediate and high R$_N$ value with high hardness and high H/E ratio shows excellent tribological performance. It can be concluded that R$_N$ has a great effect on the wear resistance of (AlCrMoSiTi)N$_x$ nitride coatings.

Fig. 10 shows the dynamic potential polarization curves of 304 SS and (AlCrMoSiTi)N high-entropy nitride coatings prepared at various N$_2$ gas flow rates in 3.5 wt% NaCl solution at RT. The Ecorr and i$_{corr}$ values obtained via the Tafel extrapolation using linear fitting are listed in Table 3. It is well known that the kinetics of corrosion resistance of the materials is usually evaluated by the i$_{corr}$ value [22], because the corrosion rate is always proportional to the i$_{corr}$. The i$_{corr}$ value was determined via extrapolating the cathodic Tafel lines to the corrosion potential [60]. The i$_{corr}$ of AlCrMoSiTi coatings is 58.5 × 10^{-8} A/cm^{-2}, and then significantly decreases to 2.2 × 10^{-8} A· cm^{-2} when the R$_N$ increases to 70%. It is worth noting that the i$_{corr}$ of the AlCrMoSiTi coatings are smaller than that of 304 SS, and this indicates that the coatings have good corrosion resistance. Moreover, the coating prepared at R$_N$ = 70% exhibit the best corrosion resistance, and its i$_{corr}$ is nearly 1/35 the value of 304 SS.

In general, the composition and microstructure of the coatings have a greater influence on their corrosion resistance [19,61]. The high i$_{corr}$ value of the AlCrMoSiTi coating maybe due to the galvanic corrosion among the target metal elements. According to the XPS results, for the (AlCrMoSiTi)N$_x$ high-entropy nitride coatings prepared under low R$_N$ values, the chemical composition of these coatings changes from metal to non-metal. However, owing to the low N content in the (AlCrMoSiTi) N$_x$ nitride coatings prepared under low R$_N$ values, the nitrides formed in these nitride coatings are unstable. Therefore, among all the nitride coatings, the non-metallicity of the (AlCrMoSiTi)N$_x$ high-entropy nitride coatings deposited at low R$_N$ values is weaker, which make the coatings prone to corrosion. With the increase of the R$_N$ value, the non-metallicity of the (AlCrMoSiTi)N$_x$ nitride coating is enhanced owing to the high N
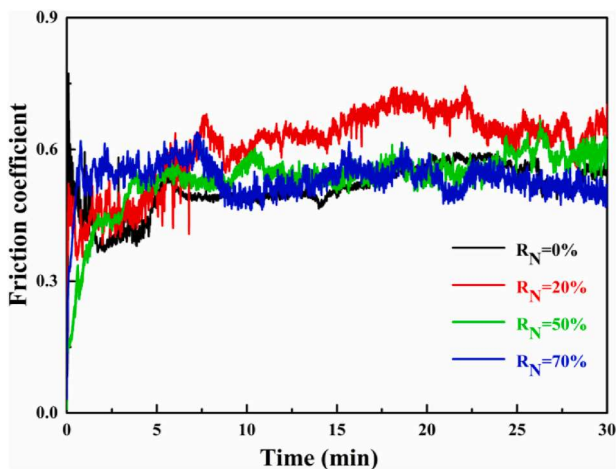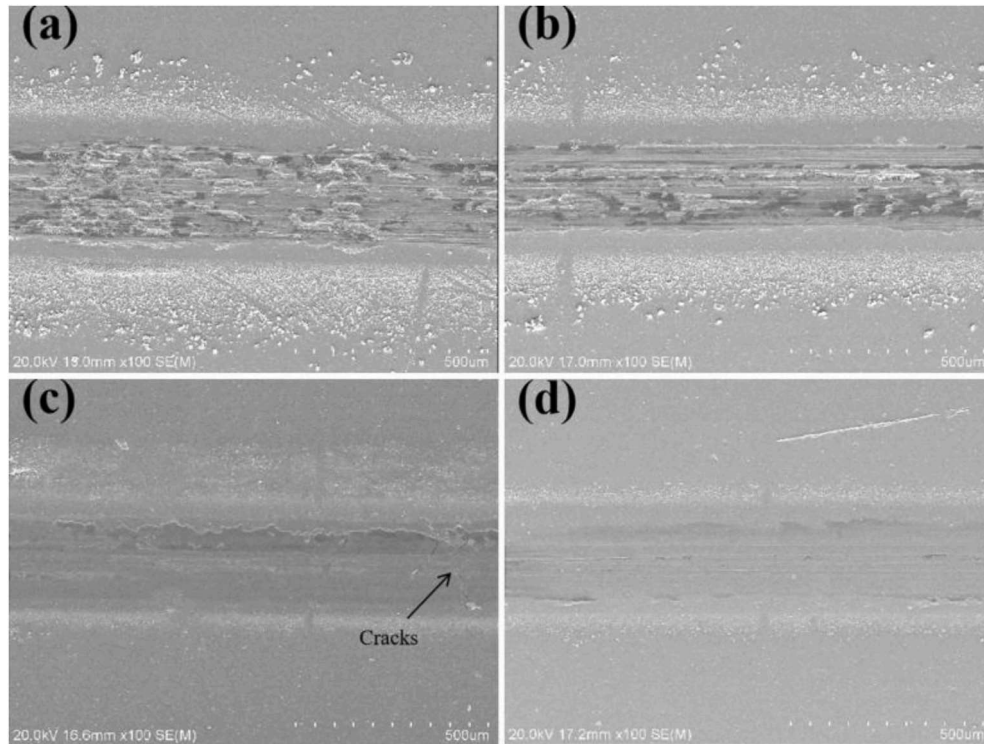

Fig. 8. Friction coefficient curves for the (AlCrMoSiTi)N$_x$ high-entropy nitride coatings prepared at various N$_2$ gas flow rates sliding in the atmosphere. All average friction coefficients of the coatings remain around 0.5, indicating that the R$_N$ has little influence on the friction coefficient of the (AlCrMoSiTi)N$_x$ high-entropy nitride coatings.

Fig. 9. SEM morphology of the wear track of (AlCrMoSiTi)N_x nitride coatings prepared at various N_2 gas flow rate: (a): 0%; (b): 20%; (c): 50%; (d): 70%. The grooves and cracks of the wear track gradually disappeared with increasing R_N.
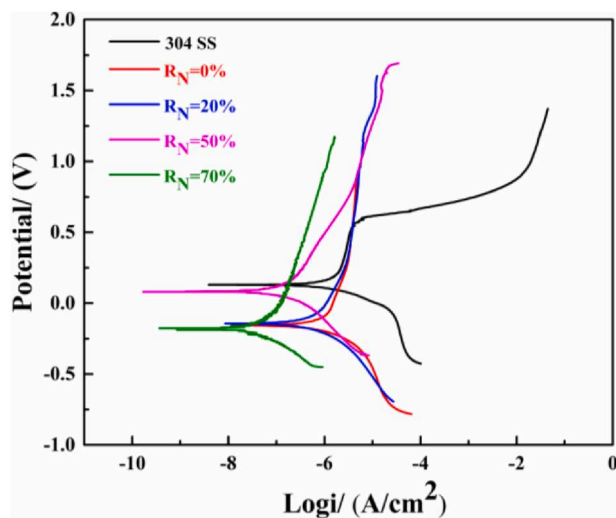

Fig. 10. Dynamic potential polarization curves of 304 stainless steel and (AlCrMoSiTi)N_x nitride coatings prepared at various N_2 gas flow rate in 3.5 wt% NaCl solution. The i_{corr} of the (AlCrMoSiTi)N_x nitride coating decreases with increasing R_N.

Table 3
The electrochemical corrosion parameters of (AlCrMoSiTi)N_x nitride coatings and 304 SS in 3.5 wt% NaCl solution.

	R_N (%)				304 SS
	0	20	50	70	
E_{corr} (V)	−0.174	−0.162	0.074	−0.196	0.116
I_{corr} (10^{-8} A cm^{-2})	58.5	38.6	7.9	2.2	78.0

content, and their corrosion resistance has been improved to a certain extent. Therefore, the coatings prepared under the $R_N = 70\%$ have the best corrosion resistance owing to the strongest non-metallic and stable chemical properties.

4. Conclusions

In this study, (AlCrMoSiTi)N_x high-entropy nitride coatings were prepared by multi-arc cathodic vacuum magnetic filtration deposition at various R_N without additional heating. The N content in the coatings increase with increasing the value of R_N, and it reaches a maximum value of 49 at. % when $R_N = 70\%$. The coatings with low N content exhibit an amorphous structure, while the coating with N content of 49 at. % present a simple FCC phase owing to the combination of the FCC-forming binary nitrides that effectively accommodates the non-FCC binary nitrides. Moreover, as the R_N increases, H, E, H/E and H^3/E^2 of the coatings all increase. At $R_N = 70\%$, the hardness of the coatings reaches a super hard level of 41.6 GPa owing to the combined effect of the formation of the strong metal-nitrogen bonding, solid solution strengthening, elevated residual stress and the grain boundary strengthening. Meanwhile, the nitride coatings exhibit low wear rate of 3.19×10^{-6} mm^3/Nm owing to the high hardness and H/E ratio. In addition, this nitride coating has low corrosion current density of 2.2×10^{-8} A cm^{-2} due to the strongest non-metallic and stable chemical properties. Thus, the tests provided evidences that the HEA nitride coating could be a potential candidate coating for mechanical tools and parts.

Declaration of competing interest

The authors declare that they have no known competing financial interests or personal relationships that could have appeared to influence the work reported in this paper.

Acknowledgment

References

[1] L.E. Toth, Transition Metal Carbides and Nitrides, Academic, New York, 1971.

[2] M. Keunecke, C. Stein, K. Bewilogua, W. Koelker, D. Kassel, H. van den Berg, Modified TiAlN coatings prepared by d.c. pulsed magnetron sputtering, Surf. Coating. Technol. 205 (2010) 1273–1278, https://doi.org/10.1016/j.surfcoat.2010.09.023.

[3] S.A. Firstov, V.F. Gorban, N.I. Danilenko, M.V. Karpets, A.A. Andreev, E. S. Makarenko, Thermal stability of superhard nitride coatings from high-entropy multicomponent Ti-V-Zr-Nb-Hf alloy, Powder Metall. Met. Ceram. 52 (2014) 560–566, https://doi.org/10.1007/s11106-014-9560-z.

[4] C.H. Lai, K.H. Cheng, S.J. Lin, J.W. Yeh, Mechanical and tribological properties of multi-element (AlCrTaTiZr)N coatings, Surf. Coating. Technol. 202 (2008) 3732–3738, https://doi.org/10.1016/j.surfcoat.2008.01.014.

[5] R.B. Li, M.X. Li, C.X. Jiang, B.W. Qiao, W.W. Zhang, J. Xu, Thermal stability of AlCrTaTiZrMo-nitride high entropy film as a diffusion barrier for Cu metallization, J. Alloys Compd. 773 (2019) 482–489, https://doi.org/10.1016/j.jallcom.2018.09.283.

[6] Q.W. Xing, H.J. Wang, M.B. Chen, Z.Y. Chen, R.B. Li, P.P. Jin, Y. Zhang, Mechanical properties and corrosion resistance of NbTiAlSiZrNx high-entropy films prepared by RF magnetron sputtering, Entropy 21 (2019) 396, https://doi.org/10.3390/e21040396.

[7] A.D. Pogrebnjak, I.V. Yakushchenko, O.V. Bondar, V.M. Beresnev, K. Oyoshi, O. M. Ivasishin, H. Amekura, Y. Takeda, M. Opielak, C. Kozak, Irradiation resistance, microstructure and mechanical properties of nanostructured (TiZrHfVNbTa)N coatings, J. Alloys Compd. 679 (2016) 155–163, https://doi.org/10.1016/j.jallcom.2016.04.064.

[8] J.W. Yeh, S.K. Chen, S.J. Lin, J.Y. Gan, T.S. Chin, T.T. Shun, C.H. Tsau, S.Y. Chang, Nanostructured high-entropy alloys with multiple principal elements: novel alloy design concepts and outcomes, Adv. Eng. Mater. 6 (2004) 299–303, https://doi.org/10.1002/adem.200300567.

[9] B. Cantor, I.T.H. Chang, P. Knight, A.J.B. Vincent, Microstructural development in equiatomic multicomponent alloys, Mater. Sci. Eng., A 375–377 (2004) 213–218, https://doi.org/10.1016/j.msea.2003.10.257.

[10] A.D. Pogrebnjak, A.A. Bagdasaryan, I.V. Yakushchenko, V.M. Beresnev, The structure and properties of high-entropy alloys and nitride coatings based on them, Russ. Chem. Rev. 83 (2014) 1027–1061, https://doi.org/10.1070/RC2014v083n11ABEH004407.

[11] J.W. Yeh, S.J. Lin, M.H. Tsai, S.Y. Chang, High-entropy Coatings, Springer International Publishing, Switzerland, 2016.

[12] W. Li, P. Liu, Peter K. Liaw, Microstructures and properties of high-entropy alloy films and coatings: a review, Mater. Res. Lett. 6 (2018) 199–229, https://doi.org/10.1080/21663831.2018.1434248.

[13] W.J. Sheng, X. Yang, C. Wang, Y. Zhang, Nano-crystallization of high-entropy amorphous NbTiAlSiWxNy films prepared by magnetron sputtering, Entropy 18 (2016) 226, https://doi.org/10.3390/e18060226.

[14] T.K. Chen, T.T. Shun, J.W. Yeh, M.S. Wong, Nanostructured nitride films of multi-element high-entropy alloys by reactive DC sputtering, Surf. Coating. Technol. 188–189 (2004) 193–200, https://doi.org/10.1016/j.surfcoat.2004.08.023.

[15] B. Ren, S.Q. Yan, R.F. Zhao, Z.X. Liu, Structure and properties of (AlCrMoNiTi)Nx and (AlCrMoZrTi)Nx films by reactive RF sputtering, Surf. Coating. Technol. 235 (2013) 764–772, https://doi.org/10.1016/j.surfcoat.2013.08.064.

[16] Y. Xu, G. Li, Y. Xia, Synthesis and characterization of super-hard AlCrTiVZr high-entropy alloy nitride films deposited by HiPIMS, Appl. Surf. Sci. 523 (2020) 146529, https://doi.org/10.1016/j.apsusc.2020.146529.

[17] V. Braic, A. Vladescu, M. Balaceanu, C.R. Luculescu, M. Braic, Nanostructured multi-element (TiZrNbHfTa)N and (TiZrNbHfTa)C hard coatings, Surf. Coating. Technol. 211 (2012) 117–121, https://doi.org/10.1016/j.surfcoat.2011.09.033.

[18] K.S. Chang, K.T. Chen, C.Y. Hsu, P.D. Hong, Growth (AlCrNbSiTiV)N thin films on the interrupted turning and properties using DCMS and HIPIMS system, Appl. Surf. Sci. 440 (2018) 1–7, https://doi.org/10.1016/j.apsusc.2018.01.110.

[19] H.T. Hsueh, W.J. Shen, M.H. Tsai, J.W. Yeh, Effect of nitrogen content and substrate bias on mechanical and corrosion properties of high-entropy films (AlCrSiTiZr)100-xNx, Surf. Coating. Technol. 206 (2012) 4106–4112, https://doi.org/10.1016/j.surfcoat.2012.03.096.

[20] Y.Q. Shen, B. Liao, Z.Q. Zhang, X.Y. Wu, M.J. Ying, X. Zhang, Anti-sand erosion and tribological performance of thick DLC coatings deposited by the filtered cathodic vacuum arc, Appl. Surf. Sci. 533 (2020) 147371, https://doi.org/10.1016/j.apsusc.2020.147371.

[21] Z.Q. Zhang, B. Liao, Y.X. Ou, F.S. Zhang, X. Zhang, Y.Q. Shen, S.N. Chen, Q.S. Hua, G.Y. He, X.P. Ouyang, Thick yet tough TiN coatings deposited by filter cathode vacuum arc technology, Acta Phys. Sin. 69 (2020) 108103, https://doi.org/10.7498/aps.69.20200036.

[22] S.N. Chen, Y.M. Zhao, Y.F. Zhang, L. Chen, B. Liao, X. Zhang, X.P. Ouyang, Influence of carbon content on the structure and tribocorrosion properties of TiAlCN/TiAlN/TiAl multilayer composite coatings, Surf. Coating. Technol. 411 (2021) 126886, https://doi.org/10.1016/j.surfcoat.2021.126886.

[23] A. Monshi, M.R. Foroughi, M.R. Monshi, Modified scherrer equation to estimate more accurately nano-crystallite size using XRD, World J. Nano Sci. Eng. 2 (3) (2012) 154–160, https://doi.org/10.4236/wjnse.2012.23020.

[24] H.S. Cao, F.G. Qi, X.P. Ouyang, N. Zhao, Y. Zhou, B.B. Li, W.Z. Luo, B. Liao, J. Luo, Effect of Ti transition layer thickness on the structure, mechanical and adhesion properties of Ti-DLC coatings on aluminum alloys, Materials 11 (2018) 1742, https://doi.org/10.3390/ma11091742.

[25] C.H. Sha, Z.F. Zhou, Z.H. Xie, P. Munroe, FeMnNiCoCr-based high entropy alloy coatings: effect of nitrogen additions on microstructural development, mechanical properties and tribological performance, Appl. Surf. Sci. 507 (2020) 145101, https://doi.org/10.1016/j.apsusc.2019.145101.

[26] N. Laegreid, G.K. Wehner, Sputtering yields of metals for Ar+ and Ne+ ions with energies from 50 to 600 eV, J. Appl. Phys. 32 (1961) 365–369, https://doi.org/10.1063/1.1736012.

[27] X.G. Feng, K.F. Zhang, Y.G. Zheng, H. Zhou, Z.H. Wan, Chemical state, structure and mechanical properties of multi-element (CrTaNbMoV)Nx films by reactive magnetron sputtering, Mater. Chem. Phys. 239 (2020) 121991, https://doi.org/10.1016/j.matchemphys.2019.121991.

[28] G. Greczynski, L. Hultman, X-ray photoelectron spectroscopy: towards reliable binding energy referencing, Prog. Mater. Sci. 107 (2020) 100591, https://doi.org/10.1016/j.pmatsci.2019.100591.

[29] G. Greczynski, L. Hultman, The same chemical state of carbon gives rise to two peaks in X-ray photoelectron spectroscopy, Sci. Rep. 11 (2021) 11195, https://doi.org/10.1038/s41598-021-90780-9.

[30] G. Greczynski, L. Hultman, Compromising science by ignorant instrument calibration - need to revisit half a century of published XPS data, Angew. Chem. Int. Ed. 59 (2020) 5002, https://doi.org/10.1002/anie.201916000.

[31] G. Greczynski, L. Hultman, Reliable determination of chemical state in x-ray photoelectron spectroscopy based on sample-work-function referencing to adventitious carbon: resolving the myth of apparent constant binding energy of the C 1s peak, Appl. Surf. Sci. 451 (2018) 99, https://doi.org/10.1016/j.apsusc.2018.04.226.

[32] K.V. Fieandt, E.M. Paschalidou, A. Srinath, P. Soucek, L. Riekehr, L. Nyholm, E. Lewin, Multi-component (Al,Cr,Nb,Y,Zr)N thin films by reactive magnetron sputter deposition for increased hardness and corrosion resistance, Thin Solid Films 693 (2020) 137685, https://doi.org/10.1016/j.tsf.2019.137685.

[33] K.V. Fieandt, L. Riekehr, B. Osinger, S. Fritze, E. Lewin, Influence of N content on structure and mechanical properties of multi-component Al-Cr-Nb-Y-Zr based thin films by reactive magnetron sputtering, Surf. Coating. Technol. 389 (2020) 125614, https://doi.org/10.1016/j.surfcoat.2020.125614.

[34] G. Greczynski, D. Primetzhofer, J. Lu, L. Hultman, Core-level spectra and binding energies of transition metal nitrides by non-destructive x-ray photoelectron spectroscopy through capping layers, Appl. Surf. Sci. 396 (2017) 347–358, https://doi.org/10.1016/j.apsusc.2016.10.152.

[35] J.F. Moulder, W.F. Stickle, P.E. Sobol, K.D. Bomben, Handbook of X-Ray Photoelectron Spectroscopy, Physical Electronics, Inc., Eden Prairie, Minn, 1995.

[36] W.L. Xie, Y.M. Zhao, B. Liao, P. Pang, D.S. Wuu, S. Zhang, Al-AlN composite coatings on AZ31 magnesium alloy for surface hardening and corrosion resistance, Vacuum 188 (2021) 110146, https://doi.org/10.1016/j.vacuum.2021.110146.

[37] D.C. Tsai, M.J. Deng, Z.C. Chang, B.H. Kuo, E.C. Chen, S.Y. Chang, F.S. Shieu, Oxidation resistance and characterization of (AlCrMoTaTi)-Six-N coating deposited via magnetron sputtering, J. Alloys Compd. 647 (2015) 179–188, https://doi.org/10.1016/j.jallcom.2015.06.025.

[38] S. Schoser, G. Brauchle, J. Forget, K. Kohlhof, T. Weber, J. Voigt, B. Rauschenbach, XPS investigation of AlN formation in aluminum alloys using plasma source ion implantation, Surf. Coating. Technol. 103–104 (1998) 222–226, https://doi.org/10.1016/S0257-8972(98)00397-1.

[39] D.C. Tsai, Z.C. Chang, B.H. Kuo, S.Y. Chang, F.S. Shieu, Effects of silicon content on the structure and properties of (AlCrMoTaTi)N coatings by reactive magnetron sputtering, J. Alloys Compd. 616 (2014) 646–651, https://doi.org/10.1016/j.jallcom.2014.07.095.

[40] B. Ren, Z.X. Liu, L. Shi, B. Cai, M.X. Wang, Structure and properties of (AlCrMnMoNiZrB0.1)Nx coatings prepared by reactive DC sputtering, Appl. Surf. Sci. 257 (2011) 7172–7178, https://doi.org/10.1016/j.apsusc.2011.03.083.

[41] H.W. Chang, P.K. Huang, A. Davison, J.W. Yeh, C.H. Tsau, C.C. Yang, Nitride films deposited from an equimolar Al-Cr-Mo-Si-Ti alloy target by reactive direct current magnetron sputtering, Thin Solid Films 516 (2008) 6402–6408, https://doi.org/10.1016/j.tsf.2008.01.019.

[42] H.W. Chang, P.K. Huang, J.W. Yeh, A. Davison, C.H. Tsau, C.C. Yang, Influence of substrate bias, deposition temperature and post-deposition annealing on the structure and properties of multi-principal-component (AlCrMoSiTi)N coatings, Surf. Coating. Technol. 202 (2008) 3360–3366, https://doi.org/10.1016/j.surfcoat.2007.12.014.

[43] D.C. Tsai, Z.C. Chang, B.H. Kuo, M.H. Shiao, S.Y. Chang, F.S. Shieu, Structural morphology and characterization of (AlCrMoTaTi)N coating deposited via magnetron sputtering, Appl. Surf. Sci. 282 (2013) 789–797, https://doi.org/10.1016/j.apsusc.2013.06.057.

[44] J. Luo, Y.X. Ou, Z.Q. Zhang, P. Pang, L. Chen, B. Liao, H.Z. Shang, X. Zhang, X. Y. Wu, Low friction coefficient of superhard nc-TiC/a-C:H nanocomposite coatings deposited by filtered cathodic vacuum arc, Mater. Res. Express 6 (2019) 096418, https://doi.org/10.1088/2053-1591/ab2e9c.

[45] D. Bootkul, N. Saenphinit, B. Supsermpol, C. Aramwit, S. Intarasiri, Synthesis of Ti-doped DLC film on SS304 steels by filtered cathodic vacuum arc (FCVA) technique for tribological improvement, Appl. Surf. Sci. 310 (2014) 293–299, https://doi.org/10.1016/j.apsusc.2014.04.053.

[46] H.S. Cao, X. Ye, H. Li, F.G. Qi, Q. Wang, X.P. Ouyang, N. Zhao, B. Liao, Microstructure, mechanical and tribological properties of multilayer Ti-DLC thick films on Al alloys by filtered cathodic vacuum arc technology, Mater. Des. 198 (2021) 109320, https://doi.org/10.1016/j.matdes.2020.109320.

[47] H.S. Cao, F.J. Liu, H. Li, F.G. Qi, X.P. Ouyang, N. Zhao, B. Liao, High temperature tribological performance and thermal conductivity of thick Ti/Ti-DLC multilayer coatings with the application potential for Al alloy pistons, Diam. Relat. Mater. 117 (2021) 108466, https://doi.org/10.1016/j.diamond.2021.108466.

[48] M.H. Tsai, C.H. Lai, J.W. Yeh, J.Y. Gan, Effects of nitrogen flow ratio on the structure and properties of reactively sputtered (AlMoNbSiTaTiVZr)N$_x$ coatings, J. Phys. D Appl. Phys. 41 (2008) 235402, https://doi.org/10.1088/0022-3727/41/23/235402.

[49] Z.C. Chang, Structure and properties of duodenary (TiVCrZrNbMoHfTaWAlSi)N coatings by reactive magnetron sputtering, Mater. Chem. Phys. 220 (2018) 98–110, https://doi.org/10.1016/j.matchemphys.2018.08.068.

[50] S. Zhang, Thin Films and Coatings: Toughening and Toughness Characterization, Crc Press, 2015.

[51] S.C. Liang, D.C. Tsai, Z.C. Chang, H.S. Sung, Y.C. Lin, Y.J. Yeh, M.J. Deng, F. S. Shieu, Structural and mechanical properties of multi-element (TiVCrZrHf)N coatings by reactive magnetron sputtering, Appl. Surf. Sci. 258 (2011) 399–403, https://doi.org/10.1016/j.apsusc.2011.09.006.

[52] B. Ren, Z.G. Shen, Z.X. Liu, Structure and mechanical properties of multi-element (AlCrMnMoNiZr)Nx coatings by reactive magnetron sputtering, J. Alloys Compd. 560 (2013) 171–176, https://doi.org/10.1016/j.jallcom.2013.01.148.

[53] K.H. Cheng, C.H. Lai, S.J. Lin, J.W. Yeh, Structural and mechanical properties of multi-element (AlCrMoTaTiZr)Nx coatings by reactive magnetron sputtering, Thin Solid Films 519 (2011) 3185–3190, https://doi.org/10.1016/j.tsf.2010.11.034.

[54] P.K. Huang, J.W. Yeh, Effects of substrate temperature and post-annealing on microstructure and properties of (AlCrNbSiTiV)N coatings, Thin Solid Films 518 (2009) 180–184, https://doi.org/10.1016/j.tsf.2009.06.020.

[55] A.D. Pogrebnjak, V.M. Beresnev, K.V. Smyrnova, YaO. Kravchenko, P.V. Zukowski, G.G. Bondarenko, The influence of nitrogen pressure on the fabrication of the two-phase superhard nanocomposite (TiZrNbAlYCr)N coatings, Mater. Lett. 211 (2018) 316–318, https://doi.org/10.1016/j.matlet.2017.09.121.

[56] A.D. Pogrebnjak, I.V. Yakushchenko, A.A. Bagdasaryan, O.V. Bondar, R. Krause-Rehberg, G. Abadias, P. Chartier, K. Oyoshi, Y. Takeda, V.M. Beresnev, O.V. Sobol, Microstructure, physical and chemical properties of nanostructured (TieHfeZreVeNb)N coatings under different deposition conditions, Mater. Chem. Phys. 147 (2014) 1079–1091, https://doi.org/10.1016/j.matchemphys.2014.06.062.

[57] A. Leyland, A. Matthews, On the significance of the H/E ratio in wear control: a nanocomposite coating approach to optimised tribological behaviour, Wear 246 (2000) 1–11, https://doi.org/10.1016/S0043-1648(00)00488-9.

[58] Y.M. Zhao, P.F. Ju, H.M. Liu, L.L. Pei, L. Ji, H.X. Li, D.S. Xue, H.D. Zhou, J.M. Chen, A strategy to construct long-range fullerene-like nanostructure in amorphous carbon film with improved toughness and carrying capacity, J. Phys. D Appl. Phys. 53 (2020) 335205, https://doi.org/10.1088/1361-6463/ab8bff (9pp).

[59] Y.Y. Chang, C.H. Chung, Tribological and mechanical properties of multicomponent CrVTiNbZr(N) coatings, Coatings 11 (2021) 41, https://doi.org/10.3390/coatings11010041.

[60] A. Aliyu, C. Srivastava, Microstructure-corrosion property correlation in electrodeposited AlCrFeCoNiCu high entropy alloys-graphene oxide composite coatings, Thin Solid Films 686 (2019) 137434, https://doi.org/10.1016/j.tsf.2019.137434.

[61] R. Chen, Z.B. Cai, J.B. Pu, Z.X. Lu, S.Y. Chen, S.J. Zheng, C. Zeng, Effects of nitriding on the microstructure and properties of VAlTiCrMo high-entropy alloy coatings by sputtering technique, J. Alloys Compd. 827 (2020) 153836, https://doi.org/10.1016/j.jallcom.2020.153836.